

UNSTEADY SEPARATED FLOW AROUND THE AHMED BODY

J. HOESSLER, JF. BEAUDOIN AND F. PEROT

PSA Peugeot Citroen, Direction of Research and Innovation, Route de Gisy, Velizy, France.
hoesslej@eleves.enpc.fr, jeanfrancois.beaudoin@mpsa.com, franck.perot@mpsa.com

Introduction

The flow around vehicles is characterized by highly turbulent and three-dimensional separations, and there is a growing need for more insight into the physical features of these dynamical flows on the one hand, and powerful numerical tools to analyse them on the other hand. In the present study we perform unsteady numerical simulations of the flow around the well-known Ahmed body (Ahmed *et al.* (1984)) using both Large Eddy Simulations (LES) and Lattice Boltzmann Method (LBM) in order to evaluate their ability to predict the mean and fluctuating flow produced by this complex geometry at high Reynolds number. From the physical point of view, we aim at analyzing both the steady and unsteady effects of the coherent structures produced in this 3D flow on the drag and lift forces applied on the body.

The Ahmed bluff body on its 25° slant angle configuration is the ideal model for our objectives as it presents a separation line and two intense and stable counter-rotating vortices on the rear slant that contribute for most of the total drag. As shown by previous numerical studies, the equilibrium between separation and streamwise vortices is very difficult to predict for such a configuration.

First of all, the configuration chosen for the two simulations as well as the numerical choices made to predict this flow are presented. It will then be shown that the results obtained are in good agreement in terms of mean flow prediction with the Laser Doppler Anemometer (LDA) measurements performed by Lienhart *et al.* (2000) on a $3/4$ open test section with a blockage ratio of 4%, an incoming velocity $U_0 = 40\text{m/s}$ and a turbulent intensity $I = 0.25\%$. Based on the length of the body $H = 1.044\text{m}$ and U_0 , the associated Reynolds number is $Re = 2.78 \times 10^6$. As a complement to these results, as this campaign covered only statistical moments, additional measurements have been performed mostly by means of hot-wire anemometry and fluctuating parietal pressure taps in order to establish a dynamical database, allowing the validation of the unsteady results obtained. These new measurements are confronted to the simulation results for studying and trying to understand the dynamical behaviour of the wake as well as its effect on forces on the rear and the slant, these two zones counting for more than 85% of the total drag according to Ahmed *et al.* (1984).

1 Presentation of the geometry

The bluff-body used is the Ahmed body on a 25° slant configuration, and its dimensions are given in fig. 1(a). The fig. 1(b) shows the CAO used for both simulations as well as the axis and frame of reference.

2 Numerical set-up

2.1 Large Eddy Simulation using *Fluent*

Large Eddy Simulations on the bluff-body using *Fluent 6.2* are performed (finite-volume method). The size of the domain is $32H \times 13.5H \times 5H$. The blockage ratio is of 2%, lower than the one used

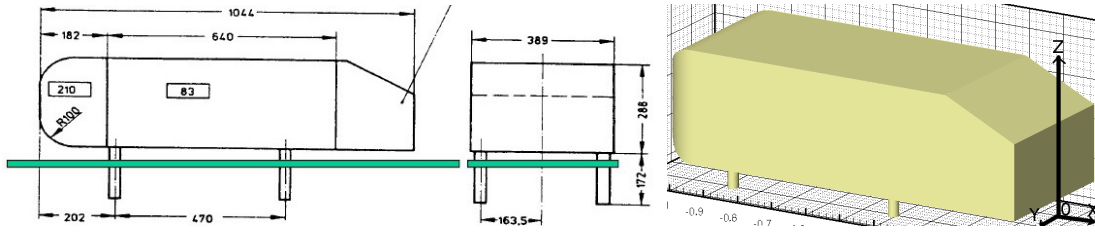


Figure 1: Ahmed bluff-body characteristics, extracted from Ahmed *et al.* (1984)(a) and CAO used for both simulations (b)

in the reference experiment. The main problem encountered was to simulate the detachment and fast reattachment of the flow after the edge between the top and the rear. As it is an high-Reynolds simulation, a log wall model is introduced in order to reduce the size of the mesh grid and to increase the time-step. The *Werner and Wengle* law (Werner and Wengle (1991)) is chosen. But as this law does not take into account the pressure gradient and thus the adverse pressure gradient encountered after the edge, the CAO has been slightly modified: the edge between the top and the slant has been rounded $R=20\text{mm}$ radius of curvature. This rounding leads to less than 5mm zone around the edge creating a smooth connection between the two faces. The hybrid unstructured grid is built as follow: the starting point is a triangular surface mesh (on the body, the associated characteristic lengths lie between 0.75mm on the edge and 4mm on the less critical zones). Lying on this mesh, 10 layers of prims in all the no-slip zones are created by extrusion, using a thickness growth of 1.2 between two consecutive layers. The thickness of the first layer is parametrized by the surface mesh and the corresponding surface resolution can be seen on fig. 2.1(c). Volume mesh is then controlled using refinement boxes as shown in fig. 2.1(a). Another projection of the volumic mesh in the $y = 0$ plane on the slant can be seen on fig. 2.1(b).

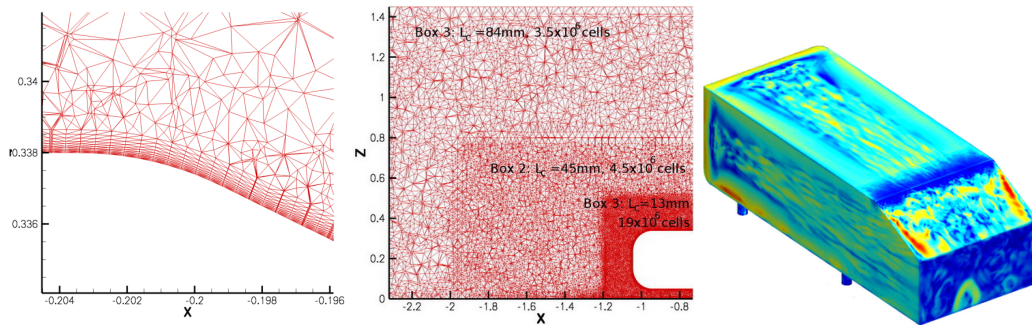


Figure 2: Projections of the mesh in the $y = 0$ plane (a,b) and contours of y^+ ($1 < y^+ < 12$)(c)

As for the boundary conditions are concerned, lateral and upper conditions are symmetry and a no-slip condition is introduced at the walls. The inlet velocity is $U_0 = 40\text{m/s}$ with a zero turbulence rate. The body is far enough from this surface to get a boundary-layer development on the floor. At the outlet, an uniform condition in pressure is applied. As for the choice of non-perturbated incoming profile, Pérot (2004) showed that adding perturbation leads to a degradation of the velocity component and pressure DSPs. Moreover, given the high size of the mesh cells in the immediately following zone and the fact that these perturbations are not spatially-correlated, they should be destroyed by either viscous or subgrid diffusion.

The last step is then to define the numerical set-up for these simulations. The segregated solver is used, meaning that the momentum and pressure equations are solved sequentially. The time ad-

vancement is performed iteratively. Moreover, the "node-based" option is used for the evaluation of velocity-gradients as it is more accurate on unstructured grids. The convection terms are evaluated using a second order bounded finite difference scheme ("bounded central differency"). For pressure, we used the second order *PRESTO!* ("PREssure STaggering Option") scheme, and the pressure-velocity coupling is performed using the *SIMPLEC* ("Semi-Implicit Method for Pressure-Linked Equation Consistent") algorithm. The time step is set to $\Delta t = 5 \times 10^{-5}s$ and 5 to 20 correction cycles are performed wether we are in the initialisation, convergence or converged phase. The subgrid-scale model chosen is the *Smagorinsky* one and the constant is equal to $C_s = 0.1$ ($\nu_{sg} = (C_s \Delta)^2 \sqrt{2\|S\|^2}$) except for the initialization of the flow (200 time-steps) during which it is set to 0.2.

2.2 Lattice-Boltzmann Simulation using *Powerflow*

The Lattice-Boltzmann (LBM) simulations are performed using *Powerflow 3.4*. This software uses a cartesian grid, with several levels of refinement. For each level, the characteristic length of cubic cells is equal to twice the length of its equivalent at the higher level. The surface mesh is then generated by projection. Nine levels of resolution are used. As in Fluent simulation, the edges are rounded and the highest resolution level is used to generate an extrusion of the slant an the close-to-edge parts of the top and the lateral faces of the body of approximately 10 cells. A same extrusion of 10 cells on all the body using a 8 resolution is then applied. The figure 2.2 shows the zones at which a level 8 (2.2.(a)) and 7 (2.2.(b)) are specified. The other levels of resolution are defined as rectangular boxes, each one containing the precedents. A law-of-the-wall is also used in which the adverse pressure gradients are modelled using a characteristic length on rounded surfaces. This characteristic length is set to the corresponding radius of curvature.

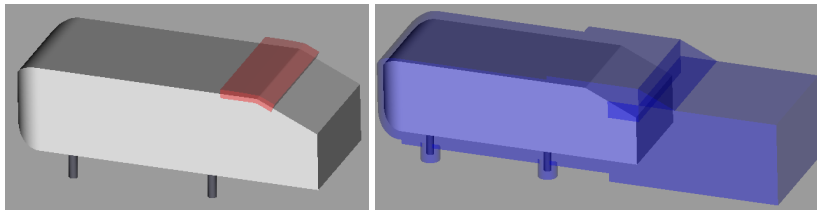


Figure 3: Resolution zones (vr) specified around the body: level 8 (a) and level 7 (b)

The time step is $\Delta t = 3.9 \times 10^{-6}s$. The characteristic length is $H_2 = 0.288m$ (height of the body without the feets), and the maximum resolution is 400, meaning that there are 400 cells for a characteristic length (the smallest characteristic length is $0.72mm$). The domain size is $76.5H_2 \times 45.8H_2 \times 55H_2$. We get a blockage ratio of 10% in the vr4 zone and 0.1% for the complete domain, once again below the experimental ratio.

3 Mean flow validation of our simulations

In order to validate the mean topology predicted by Ahmed *et al.* (1984) (two conter-rotating vortices confining a detachment bulk close to the edge), the oil streak patterns obtained by Lienhart *et al.* (2000) are compared with the friction lines obtained by simulations which are evaluated by interpolating the velocity field in a plane located at $2mm$ from the slant. The fig. 3 shows the oil streak patterns (a) and the friction lines obtained by LES and LBM simulations (resp. b and c).

The bulk is quite well predicted. The reattachement occurs slightly further upstream in LES simulations, showing better agreement with the experimental results. Yet the quality of the oil

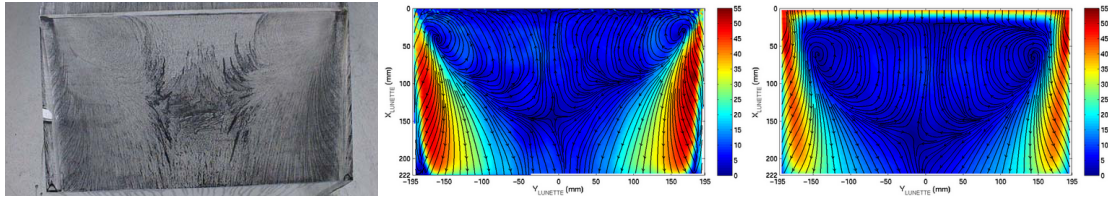


Figure 4: friction lines on the slant: Lienhart *et al.* (2000)(a), LES (b) and LBM (c) simulations

streak measurements is quite poor, making it impossible to evaluate the prediction concerning the position of the saddle point. The presence of the bulk and the two contrarotative vortices are predicted correctly (their effects can be seen on the friction lines). The next step now is to show that their interaction leads to a well predicted flow over the slant, and the fig. 3 shows that the prediction of the mean and RMS u-velocity profiles are in good agreement with the measurements of Lienhart *et al.* (2000). Once again, the LES simulation is closer to the Lienhart *et al.* (2000)

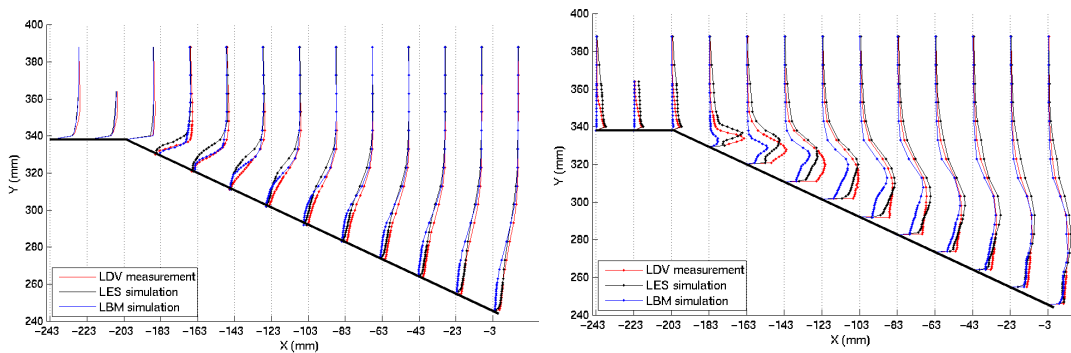


Figure 5: u-velocity profiles over the slant: mean velocity U (a) and RMS velocity U_{RMS} (b)

results, exhibiting a reattachment point upstream its corresponding LBM point. And according to the RMS velocity profiles, the reason for this late reattachment lies in a late detachment. So, as told above, predicting accurately the flow at the edge is not an easy task, and the law-of-the-wall used in Powerflow and modelling the adverse gradient in addition to the rounding of this edge seems to have caused an ill-prediction of the detachment making it occur further from the edge, leading consequently to a further reattachment. But in spite of the fact that the size and location of the recirculation bubble are not perfectly rendered, our simulations are all in all in good agreement with the experimental data, which brings us to explore the dynamical aspects with confidence.

4 Dynamical study of the wake

A time-dependant snapshot of Q-criterion contours ($Q= 5 \times 10^6$) colored by x-velocity for the LBM simulation gives an overall view of the flow in the wake (fig. 6)

The two-counter-rotating vortices as well as the structures shed around the mean detachment line can be easily identified. The latters occur further downstream than expected for a sharp edge.

Using the LES simulations, the focus is then directed at the underbody flow. We can notice the presence of a quasi-periodical spanwise recirculation bulk moving downstream at a frequency close to 60Hz. The figure 7 shows 4 instantaneous isosurfaces of zero u-velocity. This bulk seems to be the result of the interaction between the wake and the underbody flow. As the time resolution in such a simulation is too low (total simulated time simulated of approximately 1s counting

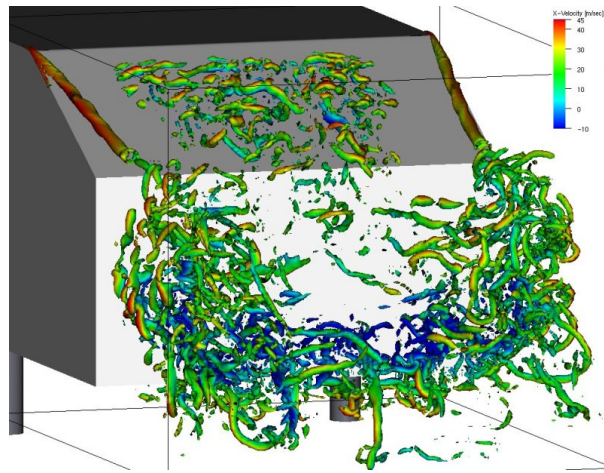


Figure 6: Instantaneous Q-criterion isosurface ($Q= 5 \times 10^6$) colored by x-velocity for the LBM simulation

the convergence phase), and given the low frequency associated to this bulk, this interaction is investigated experimentally.

First of all, the associated frequency evaluated approximately by the simulation results emerges very strongly from DSPs of hot-wire measurement in the wake lower than the slant (fig. 8). The

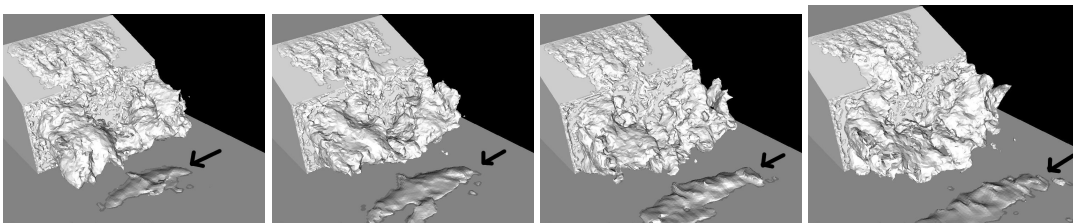
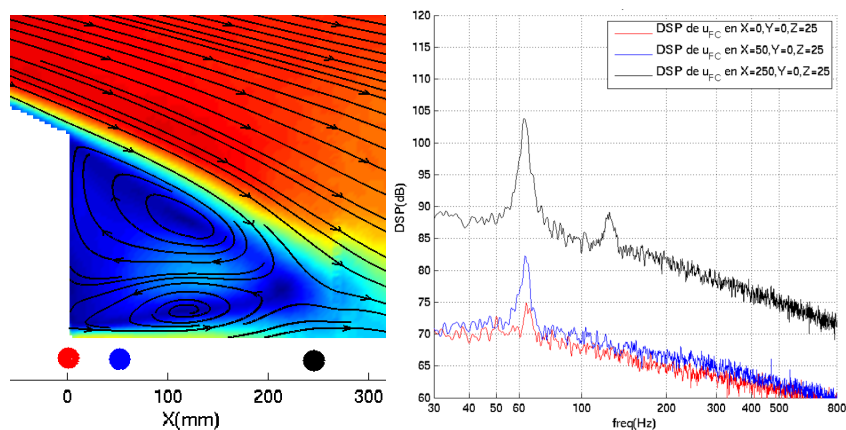


Figure 7: 4 instantaneous isosurfaces of zero x-velocity on the wake (LES simulation)



(a) Position of the hot-wire acquisition points ($y = 0$ plane) (b) corresponding DSPs of the hot-wire signals

Figure 8: Evolution of the DSPs of the U_{HW} signals in the wake zone, and close to the ground, located at $Y = 0$, $Z = 25\text{mm}$ and $X \in \{0, 50, 250\}$

amplitude of the associated peak grows with the x -coordinate and is quite low at $x = 0$, and it seems to mean that the phenomenon is localised after the end of the body. So the bulk exhibited numerically is the result of a periodical phenomenon associated to a 60Hz frequency and which seems to be provoked by the interaction of the underbody flow and the wake.

It remains now to figure whether this coherent motion has an effect on the forces generated by the flow on the body. In that aim, the fig. 9.(a) presents the location of the wall pressure taps (black dots) and hot wire probe (red dots) used for the experimental acquisitions superimposed with the mean streamlines obtained from our PIV measurements. When the hot wire is located in the underbody flow, there is a strong coherence between the measured velocity and the wall pressure on the slant (9.(b)).

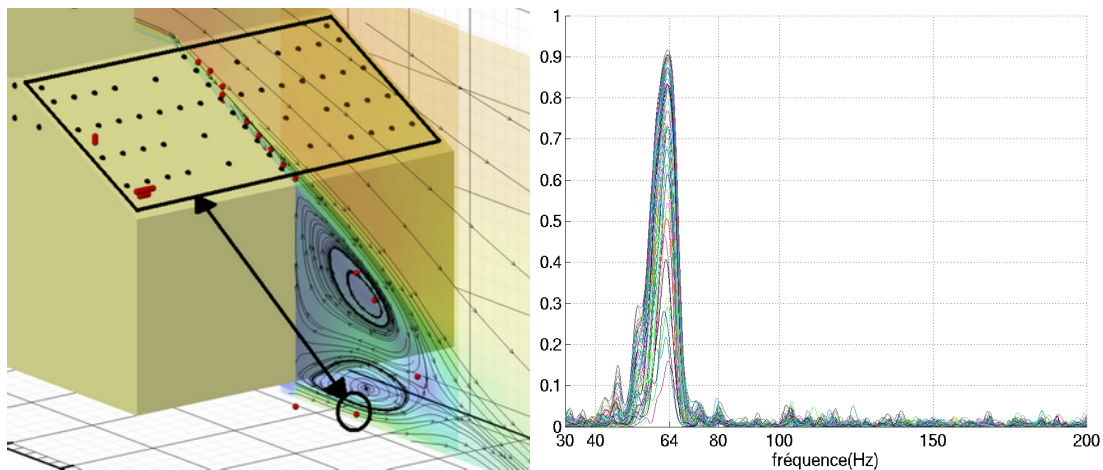


Figure 9: (a): Position of pressure taps and hot wire probe superimposed with the mean streamlines. (b): Coherence between pressure taps on the slant and the velocity measured by a hot wire probe located in the underbody flow

We believe that this phenomenon corresponds to a coherent large-scale pumping generated by the interaction between the wake and the flow coming from the underbody. And even though this coherent motion has a located origin close to the ground, at the point where the underbody flow meet the wake, it has a clear effect on all the parietal pressure taps located on the slant (and only on the slant, as there is no peak of coherence encountered when performing cross-correlation between the hot-wire signals and the taps located on the lateral parts or the top of the body).

We can thus deduce that a correct evaluation of the underbody flow to predict carefully the wake as it appears to play a key role in its dynamics, and a simulation without feet is not coherent with this necessity. If we have exhibited the fact that this pumping has an effect on the parietal pressure, the next step will be to quantify it, as well as the effect of the counter-rotating vortices.

References

- 1 AHMED *et al.* (1984): S.R AHMED, R. RAMM and G.R. FALTIN "Some salient features of the time-averaged ground vehicle wake", SAE Paper, **840300** (1995), 1–30.
- 2 LIENHART *et al.* (2000): H. LIENHART, C. STOOTTS and S. BECKER "LDA measurements of the Flow and Turbulent Structures in the Wake of a Simplified Car Model", SAE Paper, **2003-01-0656** (2000)
- 3 PÉROT (2004): F. PÉROT "Calcul du rayonnement acoustique d'écoulements turbulents bas sur des analogies acoustiques couplés aux simulations aérodynamiques instationnaires", PHD Thesis, (2004)